AIAA JOURNAL
Vol. 36, No. 6, June 1998

Radiated Noise from Airfoils in Realistic Mean Flows

David P. Lockard* and Philip J. Morris†
Pennsylvania State University, University Park, Pennsylvania 16802

The long-term objective of the research described is to use computational aeroacoustics methodology and parallel computers to increase the understanding of broadband blade noise. In a systematic progression toward simulations of completely realistic configurations and conditions, some simplified problems that address the important features of the flow are investigated. A two dimensional Navier–Stokes code, implemented using the message passing library and Fortran 90 on the IBM SP2, is used to perform the calculations. Results are presented for the interaction of a vortical gust and NACA airfoils, including nonlinear effects. The influence of gust frequency and airfoil thickness is described. A multigrid method is used to obtain converged steady-state solutions before the gust is introduced in a source region inside the domain.

Nomenclature

a_1	= vortical gust amplitude
c	= speed of sound
c_p	= pressure coefficient, $(p - p_\infty)/(1/2\rho_\infty \lvert \boldsymbol{V}_\infty \rvert^2)$
$\mathcal{D}$	= discrete form of artificial dissipation
$\mathcal{F}$	= discrete form of spatial derivatives
G	= amplification factor
h	= mesh spacing
J	= Jacobian
k	= reduced frequency
$\mathcal{L}$	= vector used in characteristic analysis
M	= Mach number
p	= pressure normalized by $\rho_\infty c_\infty^2$
p'	= perturbation pressure normalized by $\rho_\infty U_\infty a_1$
$\boldsymbol{Q}$	= vector of dependent variables
q	= heat flux
Re	= Reynolds number
T	= temperature
t	= time
U, V	= contravariant velocity components
u, v	= Cartesian velocity components
$\boldsymbol{V}$	= mean velocity vector
x, y	= Cartesian coordinates
γ	= ratio specific heats
$\kappa, \nu_{\max}, k_0, \beta_0$	= scaling coefficients for the artificial dissipation
$\boldsymbol{\Lambda}$	= vector of eigenvalues λ
λ	= eigenvalue
ν, ϕ, χ	= switches for the artificial dissipation
ξ, η	= generalized coordinates
ρ	= density

Subscripts

g	= gust
∞	= freestream quantity

Introduction

THE present paper describes the interaction of a vortical gust with a finite thickness airfoil. This problem represents an important component of methods for the prediction of broadband airfoil noise. The effects of a realistic mean flow around the airfoil on both the gust and radiated noise are included. The approach taken in this paper has several key features.

1) The mean flow is obtained from a solution of the Euler or Navier–Stokes equations. Convergence to a steady state is accelerated using a multigrid method.

2) All calculations are performed on the IBM SP2 using the message passing interface library and Fortran 90.

3) The vortical gust is generated in the interior of the computational domain. This eliminates problems at the boundaries of the computational domain.

4) A modified form of Jameson's artificial dissipation is developed that fulfills the convergence needs of the steady-state solutions as well as the nondissipative requirements of the acoustic calculations.

To perform acoustic calculations, all of the transients in the mean flow first need to be removed from the domain. If aerodynamic fluctuations persist, one is unable to identify the acoustics in the problem. This is one of the additional complications encountered when using a computational aeroacoustics (CAA) technique to simulate the interaction of a plane, vortical gust with a thick airfoil. In the current approach, a time-independent solution is obtained for the mean field, and then an unsteady disturbance is introduced to generate the gust. CAA algorithms are designed to minimize dissipation and dispersion, and so they are very inefficient at converging to a steady state. However, because it is only the spatial operators that govern the steady-state solution, any technique that uses the identical spatial operators as the CAA scheme may be used to obtain the steady solution. Hence, local time stepping with modified Runge–Kutta coefficients may be used to improve the damping characteristics and accelerate the movement of information within the domain. To further enhance the convergence, a multigrid method is employed.

Once the converged steady state is obtained, it is used as the initial flowfield in a time-accurate calculation. Although the gust could be imposed at the outer boundaries, it is generated inside the domain in a specified source region. This allows traditional boundary conditions designed to minimize reflections to be used. Inviscid calculations for two gust frequencies and several operating conditions are examined using this method. In addition, some viscous simulations have been performed to demonstrate the influence of viscous effects.

A description of the steady and unsteady algorithms is given, which emphasizes the different aims of the calculations. This includes a discussion of the boundary conditions and artificial dissipation. The multigrid method is explained, as well as all special treatments necessitated by the choice of governing equations and algorithm. Results for both unsteady and steady calculations are presented. The effects of thickness and angle of attack are also demonstrated. The unsteady cases include a comparison with results for a flat plate airfoil from previous calculations by the authors.[1] Reference 1 also includes a detailed description of the parallel implementation.

Presented as Paper 97-0286 at the AIAA 35th Aerospace Sciences Meeting, Reno, NV, Jan. 6–9, 1997; received May 28, 1997; revision received Jan. 21, 1998; accepted for publication Jan. 21, 1998.

*Graduate Research Assistant, Department of Aerospace Engineering; currently Research Scientist, NASA Langley Research Center, MS 128, Hampton, VA 23681. Member AIAA.

†Boeing/A. D. Welliver Professor, Department of Aerospace Engineering. Associate Fellow AIAA.

Numerical Algorithm

Extensive testing of computational fluid dynamics (CFD) methodology has identified high-order algorithms as the most efficient for acoustic calculations.[2] Runge–Kutta time integration and central differences in space have been chosen for the present work. In this section, the governing equations, as well as the details of the numerical scheme, are discussed.

Governing Equations

The Euler equations are normally used to describe acoustic phenomena and are used for many of the simulations in the present research. However, viscous effects may be important in the source region and also should be investigated. Therefore, some simulations presented here will use the Navier–Stokes equations. In addition, to simulate flows around curved bodies, such as airfoils, generalized coordinates are used. The fluid is assumed to be an ideal gas. The Navier–Stokes equations and the ideal gas law form a complete set of equations that can be solved for the dependent variables. These equations are made dimensionless using the speed of sound as the reference velocity. The pressure is nondimensionalized by $\rho_\infty c_\infty^2$ and the density by its freestream value. The length scale is taken to be half the airfoil chord.

The inviscid portions of the equations are written in a fully nonconservative form. However, the viscous terms are arranged to minimize the work and closely resemble the strong conservation form found in many textbooks.[3] The exact form of the equations used in this work can be found in Ref. 4. The use of the nonconservative form of the equations means that no assumptions about the metric terms are needed. Assumptions would be required to bring them inside all of the derivatives to put the equations into strong conservation form. Although certain groupings of the metric terms are identically zero analytically,[3] this result is reproduced numerically only when the metrics are calculated using the identical discretized differential operators used to solve the equations. Furthermore, the operators must not change within the domain. This is violated in the vicinity of the trailing edge of an airfoil when a grid with a C topology is used. A nonphysical source, which is generated in this region, makes it difficult to converge to steady state to machine accuracy when using a high-order scheme in conservative form. The noncompactness of the spatial operators and the low levels of dissipation in the scheme contribute to the difficulty in controlling this nonphysical source. However, a calculation of the viscous terms in a nonconservative form would be extremely costly.

Solution Algorithm

The governing equations can be placed in the semidiscrete, compact form

$$\frac{\partial \boldsymbol{Q}}{\partial t} = -[\mathcal{F}(\boldsymbol{Q}) - \mathcal{D}(\boldsymbol{Q})] = -\mathcal{R}(\boldsymbol{Q}) \tag{1}$$

Here $\mathcal{F}$ represents the discrete form of all of the spatial derivatives appearing in the governing equations. $\boldsymbol{Q}$ is the vector of the independent variables ρ, p, u, and v. Runge–Kutta time integration[5] is used to advance the solution in time. For steady-state calculations, a four-stage scheme with the coefficients [0.375, 0.5, 1.0, 1.0] is used. These coefficients give good damping characteristics over a wide range of wave numbers. This modified time-stepping algorithm is referred to as RK4. Other common choices for the coefficients do not yield any significant improvement in the stability limit for the present scheme because of the large extent of the spatial operators. The local time step is chosen based on the Courant–Freidrichs–Lewy (CFL) constraint

$$\Delta t = \frac{\mathrm{CFL}}{\left(|U| + c\sqrt{\xi_x^2 + \xi_y^2}\right) + \left(|V| + c\sqrt{\eta_x^2 + \eta_y^2}\right)} \tag{2}$$

for a CFL number of 1.1. $U = \xi_x u + \xi_y v$ and $V = \eta_x u + \eta_y v$ are the contravariant velocities. For viscous calculations, a local cell Reynold's number criterion is also satisfied.

For time-accurate calculations, the alternating five–six-stage Runge–Kutta (RK56) time integration of Hu et al.[6] is used. The smallest Δt for the entire domain is used globally. Although the method of Hu et al.[6] is technically fourth-order accurate only for linear problems, the results have been found to compare well with those from the classical fourth-order method. The primary advantage of the alternating scheme is to increase the allowable CFL number based on accuracy requirements. For the present scheme, this is 1.2, compared with 0.4 for the classical method. The spatial operator can either be sixth order or possess the dispersion-relation-preserving (DRP) property developed by Tam and Webb.[7] All of the results in this paper are obtained using the DRP coefficients given by Lockard et al.[8]

Artificial Dissipation

Central difference operators do not possess any implicit dissipation, and so a filter has been added explicitly. Because all of the spatial operators must be the same for the steady and unsteady calculations, the artificial dissipation must be appropriate for both cases. A higher-order version of the adaptive dissipation of Jameson et al.[9] has been implemented for this purpose. An optimized smoother using a seven-point stencil is used as a background dissipation rather than the fourth derivative used in the implementation of Ref. 9. This smoother, denoted by $\partial^0/\partial\xi^0$, was developed by Tam and Dong.[10]

A switch for the artificial dissipation that is more appropriate for acoustic calculations has been described by the authors.[1] This switch has been found to perform poorly for steady-state calculations because it is too sensitive to the wave number properties of the flow. A new switch that accounts for the needs of the two calculations has been implemented here. It has been used successfully to converge flows with shocks and still maintain better properties for acoustics. However, the disparity between the amplitudes of the mean flow and acoustic variables makes it extremely difficult for any switch to identify appropriately unresolved acoustic waves in the presence of strong mean flow variations. The dissipation is defined in the nonconservative form as

$$\mathcal{D} = \mathcal{D}_\xi + \mathcal{D}_\eta \tag{3}$$

where the terms in the ξ direction are

$$\mathcal{D}_\xi = \left(|U| + c\sqrt{\xi_x^2 + \xi_y^2}\right)\left(\epsilon_2 \frac{\partial^2}{\partial \xi^2} + \epsilon_0 \frac{\partial^0}{\partial \xi^0}\right)$$

$$\nu_i = \min\left(k_2, \frac{\kappa}{p_i}\frac{\partial^4 p_i}{\partial \xi^4}\right), \qquad \nu_{\max} = \max(\nu_{i-1}, \nu_i, \nu_{i+1}) \tag{4}$$

$$\epsilon_2 = \max(0, \nu_{\max} - \nu_2), \qquad \epsilon_0 = \max(0, k_0 + \phi - \epsilon_2)$$

The term ϕ is used to increase the coefficient of the basic smoother linearly in a regime when the second derivative smoother is off, but low-amplitude waves are poorly represented on the grid. It is given by

$$\phi = \chi\beta_0 k_0^{\max} \qquad \text{where} \qquad \chi = \min(\beta_1, \max(0, \nu_{\max} - \nu_0)) \tag{5}$$

$$\beta_0 = (0.1\nu_2 - \nu_0), \qquad \beta_1 = \max(0, 1/\beta_0)$$

The scaling factors β_0 and β_1 are calculated once and stored, and so they do not add much work to the calculations. In the current implementation, $\kappa = 0.3$ is a scaling coefficient for the switch and $k_0 = 1e-3$ is the background level of the basic smoother. The background smoother begins increasing above its background level when the switch exceeds $\nu_0 = 1e-5$. Also, $k_0^{\max} = 0.01$ is the maximum allowable value of the background smoother, k_2 fixes the maximum allowable value of the second-derivative dissipation and is set to 0.17, and $\nu_2 = 0.02$ defines a threshold value below which no second-order dissipation is used.

At boundaries, the dissipation stencil is decreased from seven to five and then to three points. No dissipation is applied normal to a boundary on grid lines that represent inflow and outflow boundaries. However, along a grid line representing a solid wall, the dissipation is of equal magnitude but sign opposite to that of the points of the adjacent grid line. The scaling coefficient at the wall and at the adjacent points is 0.03. The fourth and sixth derivatives use 0.02 and 0.01, respectively. It is believed that the method of characteristic boundary conditions employed in this research has a significant impact on the optimal choice of dissipation near the wall.

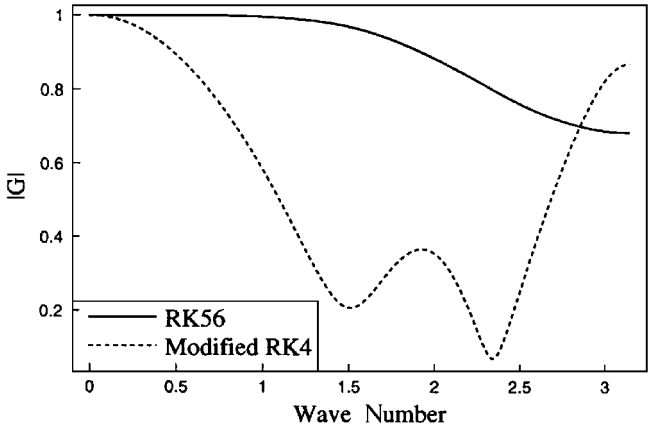

a) Amplification factors

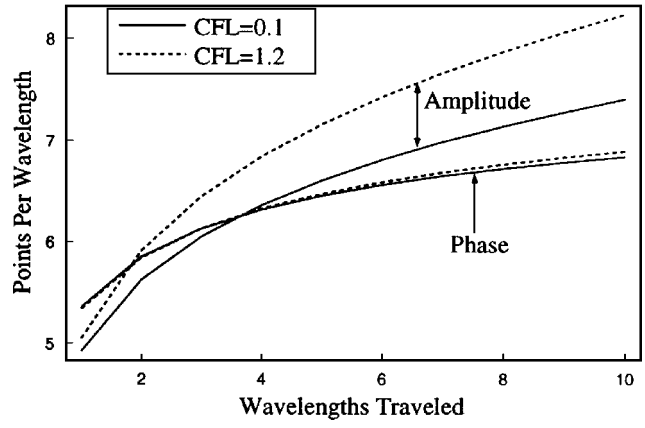

b) PPW analysis of RK56

Fig. 1 Comparison of amplification factors and PPW requirements; dissipation coefficient $k_0 = 0.001$; error tolerance for PPW analysis is 5%.

Algorithm Performance

To illustrate the performance characteristics of the schemes, Fig. 1a shows the results of a von Neumann stability analysis. The magnitude of the amplification factor $|G|$ is the ratio of the amplitude of the solution at successive time steps. Hence, Fig. 1a shows that the modified RK4 scheme has considerably more dissipation over most of the wave number regime. The points per wavelength (PPW) analysis[8] in Fig. 1b gives an estimate of the required number of points per wavelength needed to achieve a prescribed level of accuracy after a wave has propagated a given distance. Figure 1b shows that the RK56 scheme requires more points to satisfy the amplitude criterion, which is controlled by dissipation. However, reducing the dissipation coefficient fails to eliminate quickly the odd–even oscillations generated by waves entering a region where they are underresolved. Nonetheless, the performance is good for CFL numbers ranging from 0.1 to 1.2. In unsteady calculations the CFL condition is applied to the smallest cell, so that most of the domain uses a CFL number that is smaller than the prescribed maximum value of 1.2.

Boundary Conditions

Nonreflecting boundary conditions are necessary for acoustic simulations inasmuch as nonphysical reflections of waves into the computational domain can alter the solution significantly. For steady-state calculations, boundary conditions should not alter the mean aerodynamics while minimizing reflections that inhibit convergence. In the present steady-state calculations, Riemann invariant[5] boundary conditions are used at inflow boundaries. Thompson[11]-type conditions have been applied in grid-aligned coordinates at outflow boundaries.

In unsteady calculations it is extremely important to minimize reflections. Here, conditions for a nonuniform mean flow proposed by Tam and Dong[10] are used. This method essentially linearizes the Bayliss and Turkel[12] B_1 operator and the Euler equations around a nonuniform mean flow. These equations have been applied in a one-point region surrounding the computational domain.

At solid walls it is common practice to apply a condition to the normal pressure gradient and extrapolate all other variables to the wall. In an effort to better simulate the density and velocity variations near the wall, the conditions developed by Thompson[11] are applied by decomposing the equations in the direction normal to the wall. After application of a series of matrix manipulations outlined by Thompson,[11] the governing equations become

$$\boldsymbol{S}^{-1}\frac{\partial \boldsymbol{Q}}{\partial t} + \mathcal{L} + \boldsymbol{S}^{-1}\boldsymbol{C} = 0 \tag{6}$$

For a two-dimensional problem decomposed in the ξ direction, the relevant quantities are

$$\boldsymbol{\Lambda} = \{U - |\nabla\xi|c,\ U,\ U,\ U + |\nabla\xi|c\}^T \tag{7}$$

$$\mathcal{L} = \begin{Bmatrix} \lambda_1\left\{|\nabla\xi|\dfrac{\partial p}{\partial \xi} - \rho c\left(\xi_x\dfrac{\partial u}{\partial \xi} + \xi_y\dfrac{\partial v}{\partial \xi}\right)\right\} \\ \lambda_2\left(-\dfrac{\partial p}{\partial \xi} + c^2\dfrac{\partial \rho}{\partial \xi}\right) \\ \lambda_3\left(-\xi_y\dfrac{\partial u}{\partial \xi} + \xi_x\dfrac{\partial v}{\partial \xi}\right) \\ \lambda_4\left\{|\nabla\xi|\dfrac{\partial p}{\partial \xi} + \rho c\left(\xi_x\dfrac{\partial u}{\partial \xi} + \xi_y\dfrac{\partial v}{\partial \xi}\right)\right\} \end{Bmatrix} \tag{8}$$

$$\boldsymbol{S}\mathcal{L} = \begin{Bmatrix} \dfrac{\mathcal{L}_1 + 2|\nabla\xi|\mathcal{L}_2 + \mathcal{L}_4}{2c^2|\nabla\xi|} \\ \dfrac{\mathcal{L}_1 + \mathcal{L}_4}{2|\nabla\xi|} \\ \dfrac{\xi_x(\mathcal{L}_4 - \mathcal{L}_1) - 2\rho c\xi_y\mathcal{L}_3}{2\rho c|\nabla\xi|^2} \\ \dfrac{\xi_y(\mathcal{L}_4 - \mathcal{L}_1) + 2\rho c\xi_x\mathcal{L}_3}{2\rho c|\nabla\xi|^2} \end{Bmatrix}$$

The subscripts on λ represent the elements of the vector $\boldsymbol{\Lambda}$. In this form, the direction of propagation of the characteristic variables $\boldsymbol{S}^{-1}\partial\boldsymbol{Q}$ along ξ is governed by $\mathcal{L}$. At a boundary, those variables propagating out of the domain are updated using information from within the computational domain, whereas all others are specified. At a wall in inviscid flow, the equations simplify greatly because of the no-penetration condition. In this case, $\mathcal{L}_2 = \mathcal{L}_3 = 0$. The signs on $\mathcal{L}_1$ and $\mathcal{L}_4$ are opposite, and so one will be calculated and one needs to be specified. The new feature in the current approach is to use all of the terms in the momentum equations to determine the $\mathcal{L}$ representing the incoming wave to force the normal velocity U to remain zero. The no-penetration condition is

$$\frac{\partial U}{\partial t} = \xi_x\frac{\partial u}{\partial t} + \xi_x\frac{\partial v}{\partial t} = 0 \tag{9}$$

Replacing the time derivatives of u and v with the appropriate terms from Eq. (6) leads to

$$\mathcal{L}_1 - \mathcal{L}_4 = (2\rho c)(\xi_x C_3 + \xi_y C_4) \tag{10}$$

which provides an equation for the unknown $\mathcal{L}$. C_3 and C_4 include all of the tangential and viscous terms in the u and v momentum equations, respectively. Although this method applies a condition to the normal derivative of the pressure, as do many other methods, it also provides information on the evolution of the other flow variables. For a plane wall in inviscid flow, the right-hand side of Eq. (10) is zero, which reduces to the result obtained by Thompson.[11] The conditions are implemented using third-order, fully biased operators in the wall normal direction. Because the artificial dissipation terms generate a normal velocity at the wall, this is subtracted off after each Runge–Kutta stage. In practice, we have found that the pressure from the characteristic approach is very similar to that obtained using the conventional method, but some deviation is observed in the other variables. Although some additional coding is required for the characteristic approach, it attempts to model the physics

near the wall to solve for all of the unknowns. The traditional approach applies a low-order extrapolation, which is clearly incorrect. However, a zeroth-order extrapolation can have a stabilizing effect, which may be lost by the characteristic approach. When the mesh is very fine near the body, the error introduced by the extrapolation is small. Thus, the characteristic approach is likely to be most useful on meshes less dense than those used for traditional CFD, which is often the case in CAA. The points along the cut line of the C-type grid, with stencils that extend onto the airfoil, must also be treated carefully. The $\boldsymbol{Q}$ at these points are replaced by the average of the upper and lower solutions along the cut after each stage.

Multigrid Acceleration

Jameson's[13] full approximation storage method extends multigrid techniques to accelerate time-marching algorithms to converge more efficiently to the steady state of the Euler and Navier–Stokes equations. The current implementation most closely resembles the finite difference code described by Chima et al.[14] Ozyoruk and Long[15] recently reported on the adaptation of a spatially fourth-order CAA algorithm to employ a multigrid technique, but their implementation more closely resembles a finite volume development.

Basic to any multigrid scheme are transfer operators. $\mathcal{W}_h^{2h}$ denotes restriction from a fine mesh to a coarse mesh. Subscripts are used to denote the mesh spacing with h representing the fine mesh and $2h$ the coarse mesh. The full weighting operator[16] is used to restrict the residual. In addition, the Jacobian is used as a weighting factor. This is somewhat implicit when the equations are solved in conservative form. Thus, $\mathcal{R}_{2h} = \mathcal{W}_h^{2h}\mathcal{R}_h$ can be expressed in one dimension as

$$\frac{\mathcal{R}_{2h}^{i}}{2J_{2h}^{i}} = \frac{1}{4}\left(\frac{\mathcal{R}_h^{2i-1}}{J_h^{2i-1}} + 2\frac{\mathcal{R}_h^{2i}}{J_h^{2i}} + \frac{\mathcal{R}_h^{2i+1}}{J_h^{2i+1}}\right) \tag{11}$$

The superscript denotes the grid point, and i ranges from 0 to $N/2-1$. N represents the grid size on the fine mesh. In two dimensions the restriction operator is a simple generalization into a nine-point operator with the most distant points weighted by $\frac{1}{16}$, adjacent points by $\frac{1}{8}$, and the center point by $\frac{1}{4}$. The scaling parameter on the Jacobian on the left-hand side also increases from 2 to 4. Near boundaries, all points from outside the domain that would be used in the restriction are defined to be the values at the adjacent point in the grid. Also, any special operations that are performed on the solution variables after each Runge–Kutta stage must be properly reflected in the fine-grid residual before restriction. For example, the residual on inviscid walls must be tangent to the wall before the restriction operation. Direct injection is used for the solution variables $\boldsymbol{Q}_{2h}^{i,j} = \boldsymbol{Q}_h^{2i,2j}$. Furthermore, all grid parameters, such as the metrics, are restricted by simply scaling directly injected values. For example, $J_{2h}^{i,j} = \frac{1}{4}J_h^{2i,2j}$.

$\mathcal{I}_{2h}^{h}$ signifies prolongation from a coarse to a fine mesh. It is applied only to the correction to the solution. This correction is the difference between the current solution on the coarse mesh and the starting one obtained by restricting the fine-grid solution. The correction after n time steps on a coarse mesh is given by $\Delta\boldsymbol{Q}_{2h} = \boldsymbol{Q}_{2h}^{(n)} - \mathcal{W}_h^{2h}\boldsymbol{Q}_h$. Points that coincide are injected directly. All other points on the fine mesh are found using bilinear interpolation[16] of the coarse-grid corrections. The solution on the fine mesh is then modified by $\boldsymbol{Q}_h^{\text{new}} = \boldsymbol{Q}_h + \Delta\boldsymbol{Q}_h$.

By using these operators to transfer information between meshes, a multilevel algorithm may be implemented. The stages of the RK scheme on a coarse mesh are given by

$$\boldsymbol{Q}_{2h}^{(s)} = \boldsymbol{Q}_{2h}^{(0)} - \alpha_s \Delta t_{2h}\left[\mathcal{F}\left(\boldsymbol{Q}_{2h}^{(s-1)}\right) - \mathcal{D}\left(\boldsymbol{Q}_{2h}^{(0)}\right) + \mathcal{P}_{2h}\right] \tag{12}$$

where $\mathcal{P}_{2h}$ is a forcing function defined by

$$\mathcal{P}_{2h} = \mathcal{W}_h^{2h}[\mathcal{F}_h(\boldsymbol{Q}_h) - \mathcal{D}_h(\boldsymbol{Q}_h)] - \left[\mathcal{F}_{2h}\left(\boldsymbol{Q}_{2h}^{(0)}\right) - \mathcal{D}_{2h}\left(\boldsymbol{Q}_{2h}^{(0)}\right)\right] \tag{13}$$

Because the forcing function contains the residual of the coarse mesh from the first RK stage, the solution on the coarse mesh will be driven by the fine-grid residual. This can be exploited by using a different scheme on coarser meshes. A second-order, central difference spatial operator with a constant-coefficient, second-derivative dissipation is used on all coarse meshes. This allows the CFL number to be increased on coarser meshes and further reduces the work while maintaining the spatial accuracy on the fine mesh.

The process may be repeated for as many meshes as desired, but only a maximum of four levels have been used successfully with the current code. The finest mesh is chosen to have $2n+1$ points in each direction, where n is an integer. This allows the boundaries to be maintained as the grid is reduced. A saw-toothed cycle is used with two Runge–Kutta iterations on the coarsest mesh and one on all other meshes. After every restriction and prolongation of the solution variables, all boundary conditions are applied. The solution is started on the finest mesh, with the saw-toothed cycles continuing until convergence to machine accuracy is obtained.

Results

Mean Flow Solutions

Although the current approach is general enough to handle a wide variety of airfoil shapes, the NACA00 family is used because they are similar to the symmetric airfoils used in some previous studies of gust interaction noise.[17] Figure 2 shows the Mach number distribution and grid for a NACA0012 airfoil. The angle of attack α is zero, and the freestream Mach number is 0.5. The grid is of C topology, with the first number in the dimensions 81×129 representing the number of C curves. The outer grid boundaries are relatively close to the airfoil, but highly stretched grids have been found to perform poorly for unsteady calculations. Figure 3 gives the convergence history for this case. Multigrid acceleration reduces the number of cycles by a factor of 10, but the overhead in work reduces the actual savings. These calculations have been performed on an IBM SP-2 with 4–16 nodes. The time in Fig. 3 has been converted to

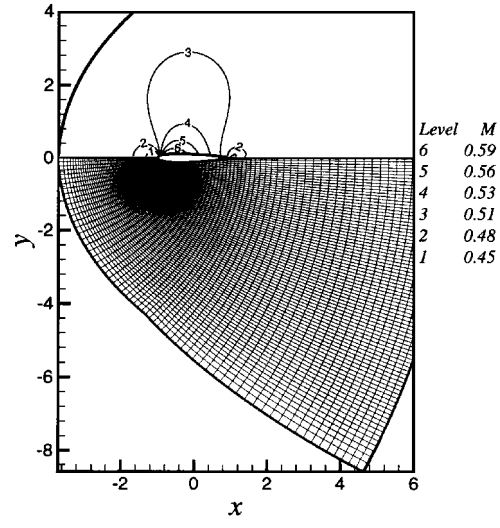

Fig. 2 Mach number distribution and 81 × 129 grid for a NACA0012 airfoil; $M = 0.5$ and $\alpha = 0$ deg.

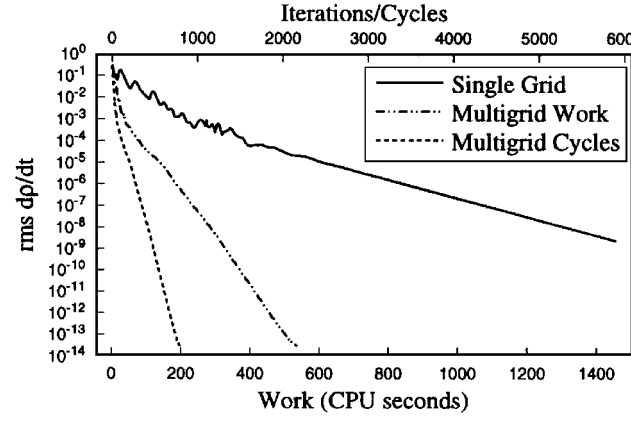

Fig. 3 Convergence history for a NACA0012 airfoil on an 81 × 129 grid; $M = 0.5$ and $\alpha = 0$ deg.

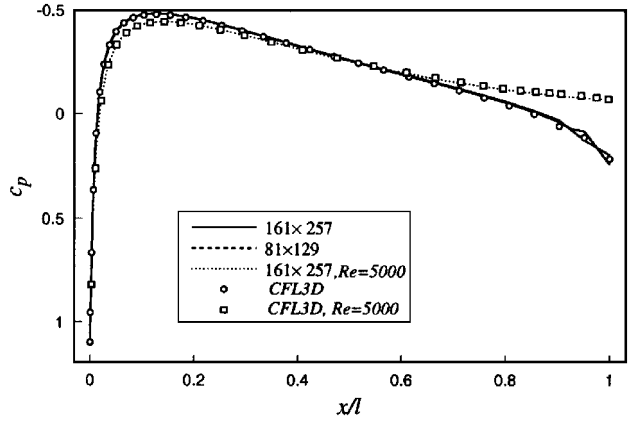

Fig. 4 Surface pressure distribution for a NACA0012 airfoil; $M = 0.5$ and $\alpha = 0$ deg.

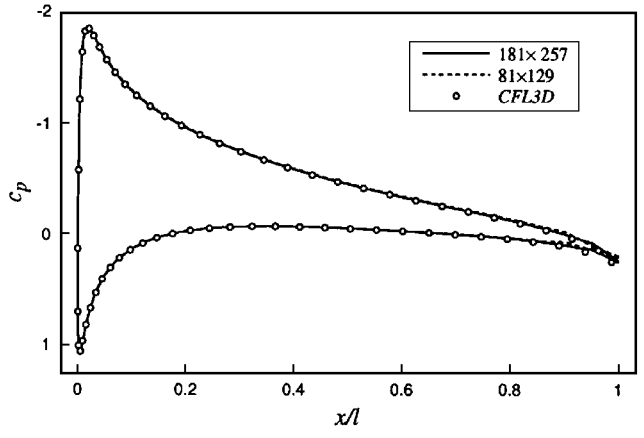

Fig. 5 Surface pressure distribution for a NACA0012 airfoil; $M = 0.5$ and $\alpha = 5$ deg.

equivalent single-node CPU time. More nodes could have been used, but the problem size did not warrant it. Flows with lifting airfoils and shocks converged more slowly, but the savings were similar.

Figures 4 and 5 give grid refinement studies of the surface pressure distributions for the NACA0012 at $\alpha = 0$ and 5 deg, respectively. The mean flow solutions have been validated through grid refinement studies and comparisons with experimental data and production CFD codes. The symbols represent the solution from the code CFL3D.[18] Fine grids clustered near the body were used with CFL3D, and so only a few of the data points from those calculations are included. There is very little difference between the solutions from the grid refinement and CFL3D. However, some discrepancy can be seen near the trailing edge. The abrupt change in the boundary condition at the trailing edge gives rise to a small pressure jump that generates some oscillations. Figure 4 also shows that a viscous calculation with $Re = 5 \times 10^3$ for the $\alpha = 0$ deg case reduces these fluctuations significantly. The viscous terms model the physics in this region more accurately, but the solution is still not perfectly smooth.

Airfoil/Gust Interaction

The primary goal of the present research is to simulate the noise radiated when unsteady disturbances encounter solid bodies. Because it is difficult to impose arbitrary disturbances at curved boundaries and still minimize reflections of outgoing waves, an alternate approach has been developed to generate the gust inside the domain. To make comparisons with other work in this area, a plane vortical disturbance of the form

$$v = a_1 \cos[k(x - Mt)] \tag{14}$$

is introduced inside the domain by adding a source function to the governing equations. The source is derived by finding a suitable forcing function for the equations that produces the desired form for the gust. Because the gust is incompressible and vortical, only the momentum equations need to be modified. By assuming that the source is in a region of uniform flow in the x direction and interactions between the gust and other waves are negligible, one obtains

$$\frac{\partial u_g}{\partial t} + M\frac{\partial u_g}{\partial x} = \frac{\partial S}{\partial y}, \qquad \frac{\partial v_g}{\partial t} + M\frac{\partial v_g}{\partial x} = -\frac{\partial S}{\partial x} \tag{15}$$

The subscript g refers to the gust. A solution for S is sought that produces a gust of the form of Eq. (14) downstream of the source. The equations for the total field are then modified to include the source in the form

$$\frac{\partial u}{\partial t} \cdots = \frac{\partial \Psi}{\partial y}\sin(kMt), \qquad \frac{\partial v}{\partial t} \cdots = -\frac{\partial \Psi}{\partial x}\sin(kMt) \tag{16}$$

where

$$\Psi = a_1 \frac{M(b^2 - k^2)}{4b^2 \sin(k\pi/b)}\{1 + \cos[b(x - x_0)]\}\{\tanh[3(y + y_0)] - \tanh[3(y - y_0)]\} \tag{17}$$

in the range $|x - x_0| < \pi/b$, where x_0 and y_0 specify the center of the source and b specifies its width. The source is similar to a stream function so that the induced vortical gust velocities are solenoidal to linear order. Thus, the gust should not produce any noise. Here, $k = \omega l/(2U_\infty)$ is the reduced frequency and $l/2$ is the chord half-length, which is the reference length. Thus, the airfoil always extends from -1 to 1. After a periodic steady state is reached, the perturbation pressure is sampled over several periods to obtain rms values. Similar data for a flat plate have been compared to the semianalytic results of Atassi et al.[19] in an earlier paper.[1] Atassi et al.[20] have also presented results for thick Joukowski airfoils. Agarwal and Huh[21] also performed calculations for similar flows. Myers and Kerschen[22] and Howe[23] have developed analytic techniques for gust interaction problems. To be consistent with previously published results, the rms values are multiplied by $\sqrt{2}$ to obtain the amplitude of the oscillations $|p'|$. A gust amplitude of $a_1 = 1e - 3$ is used in all of the studies. Although the amplitude is small, the calculations are fully nonlinear. Also, many of the comparisons use $\rho_\infty U_\infty a_1$ to normalize the perturbation pressure. This dimensionless pressure is denoted by p' to distinguish it from the total pressure p normalized by $\rho_\infty c_\infty^2$ in the CAA code.

An example of the instantaneous v velocity contours is given in Fig. 6 to demonstrate that the method is capable of generating a periodic gust. In this case, $x_0 = -2.5$, $y_0 = 1.5$, and $b = 5$. Good results have been obtained for a variety of frequencies and amplitudes as long as the sine function in the definition of Ψ does not approach zero. When this occurs, large internal cancellations take place that can lead to large amplitudes and poorly resolved waveforms within the source region. A shear layer in the streamwise velocity is generated in the region where the hyperbolic tangent functions vary. This region is susceptible to instabilities and spreading by the artificial dissipation. However, the noise emanating from

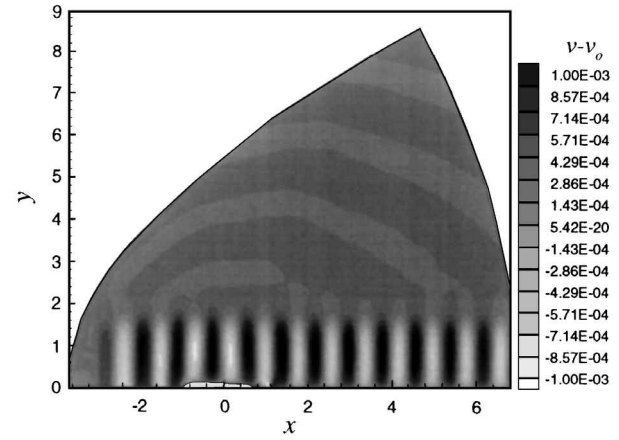

Fig. 6 Instantaneous v contours for a NACA0012 airfoil; $k = 7.85$, $M = 0.5$, and $\alpha = 0$ deg.

this region is usually relatively small. Furthermore, instabilities and further alterations to the gust that result from interactions with the nonuniform mean flow and acoustic waves actually model real fluid effects. The inability of the present method to simulate an infinite, periodic gust perfectly should not be viewed as a limitation. In fact, these mechanisms need to be simulated properly to solve a more complete, realistic problem than the simple, single-frequency gust interactions described here.

Low Frequency

A reduced frequency of $k = 1$ is used with a freestream Mach number of 0.5 to correspond to the conditions used for a flat plate airfoil in our earlier paper.[1] It was shown that the CAA results for a flat plate are similar to the semianalytic solution of Atassi et al.[19] Unfortunately, no comparison solutions by other methods are available for the airfoils used in the present study. Therefore, only CAA results will be given in the following presentation, with qualitative comparisons being made to similar calculations by others. Besides the change in position of the solid surface, the thick-airfoil calculations also include a nonuniform mean flow, which may distort the gust and acoustics.

Figures 7 and 8 demonstrate the effect of thickness on the radiated noise and surface pressure magnitude. In the directivity plot, r is the polar distance from the origin to the observer. The angle θ is always measured from the airfoil axis. At zero angle of attack, $\theta = 0$ corresponds to the freestream direction. The amplitude of the pressure oscillation for any angle is given by the distance to the point on the corresponding curve. Only the upper half-plane is given for $\alpha = 0$ deg cases because the rms values possess symmetry across $y = 0$. However, both upper and lower planes are used in all of the computations. Both of the solutions for the NACA airfoils show increased noise radiation in the upstream direction. However, note that the directivities are obtained directly from rms data along a grid line within the domain. The directivity plots scale the data by $\sqrt{r}$ to account for the cylindrical spreading, which is correct only in the far field. Some additional variation with radial distance has been observed from the numerical solutions, indicating that the grid does not extend to the far field. A Kirchhoff-type integral technique could

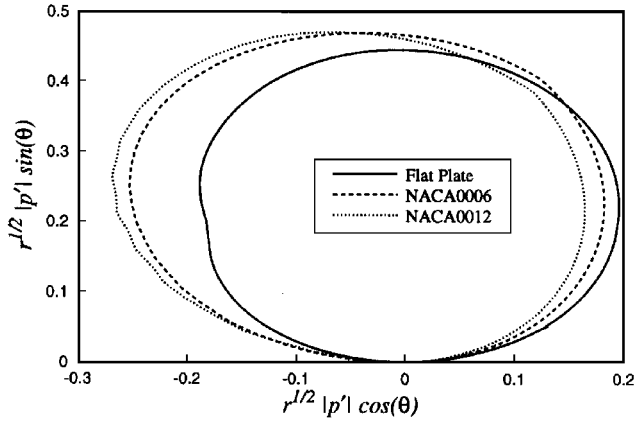

Fig. 7 Directivity variation with thickness; $k = 1$, $M = 0.5$, and $\alpha = 0$ deg.

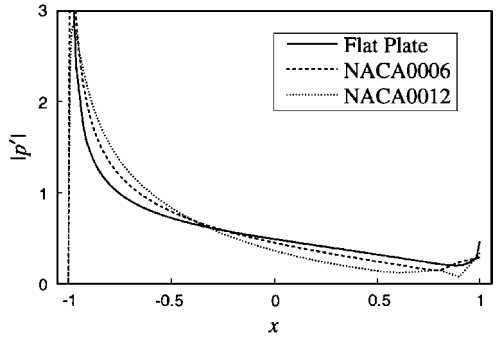

Fig. 8 Surface pressure magnitude variation with thickness; $k = 1$, $M = 0.5$, and $\alpha = 0$ deg.

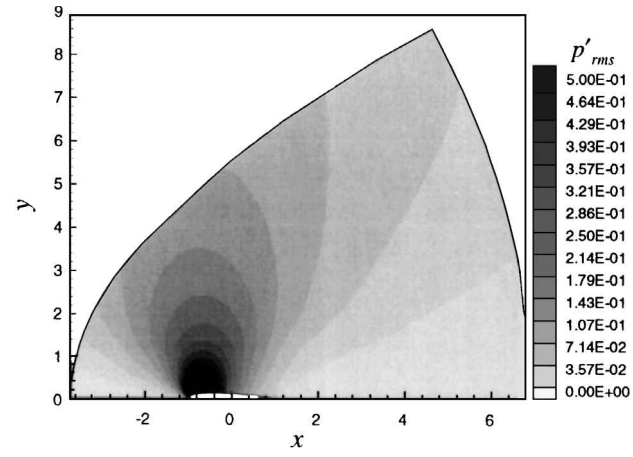

Fig. 9 NACA0012 airfoil rms pressure contours; $k = 1$, $M = 0.5$, and $\alpha = 0$ deg.

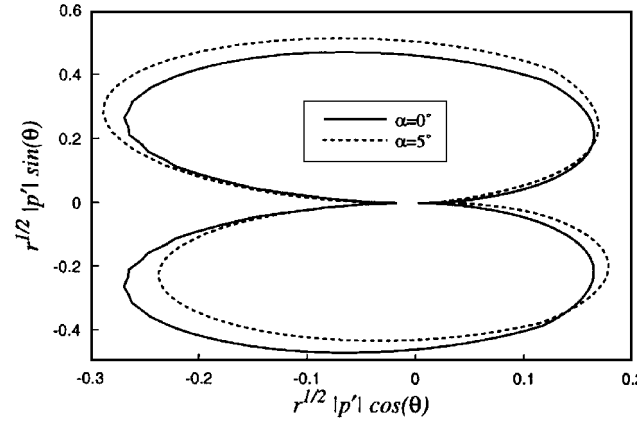

Fig. 10 Directivity variation with angle of attack for a NACA0012 airfoil; $k = 1$ and $M = 0.5$.

be used to obtain true far-field values because it would require enormous resources to extend the grid until all of these variations disappeared; however, the trend with thickness is consistent with the work of Atassi et al.[20] The surface pressures in Fig. 8 indicate that the dominant noise source is near the leading edge. Similar to the mean flow result, a jump in the pressure amplitude is visible in the vicinity of the trailing edge. The pressure variations for the airfoils go to zero at the stagnation point as expected. Figure 9 shows that the noise is primarily radiated normal to the airfoil from near the leading edge. The airfoil calculations are fairly well converged, as unsteady solutions on the 81×129 and 161×257 grids show little change. In the case of the flat plate, the singularity at the leading edge makes it very difficult to obtain consistent results with grid refinement. At this low frequency, the wavelengths of the unsteady disturbances are longer than the airfoil chord. Hence, they are overresolved even on the coarse mesh. The acoustic wavelength is so long that the scale for the mean flow actually governs the required grid spacing.

The effect of the angle of attack is shown in Figs. 10 and 11. The radiated noise is augmented on the suction side, $y > 0$, and decreased on the pressure side. This is seen in both the directivity and pressure amplitude plots.

A calculation has also been made for a viscous flow at a $Re = 5000$ and $\alpha = 0$ deg for a NACA0012 airfoil. The directivity in Fig. 12 is similar to the inviscid case except in the downstream direction. This is caused by a slight instability in the viscous wake triggered by the gust. At higher frequencies the instabilities grow rapidly and cause variations comparable to those of the mean flow. However, at this low gust frequency, the wake dynamics do not appear to alter the sound field significantly. Figure 13 shows that the surface pressure amplitudes are also consistent. However, the viscous calculation does not exhibit any spike at the trailing edge. Thus, the viscosity applies a pressure condition that incorporates some of the flow physics absent in the inviscid case.

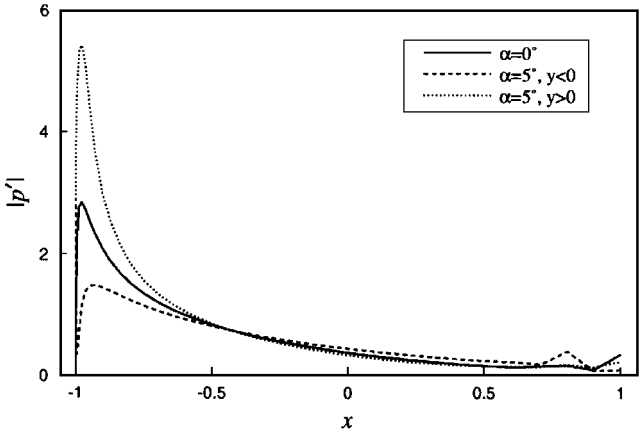

Fig. 11 Surface pressure magnitude variation with angle of attack for a NACA0012 airfoil; $k = 1$ and $M = 0.5$.

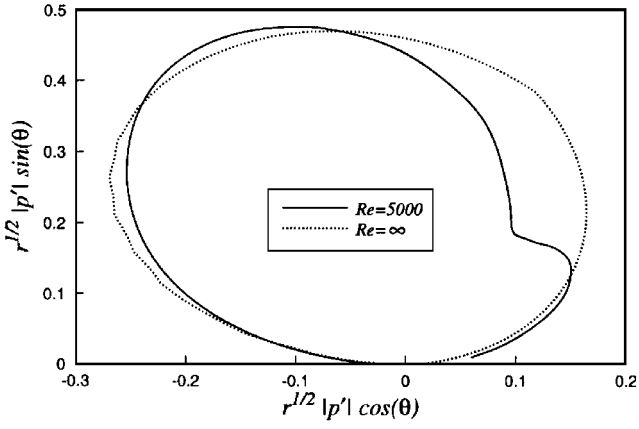

Fig. 12 Directivity variation with Reynolds number for a NACA0012 airfoil; $k = 1, M = 0.5$, and $\alpha = 0$ deg.

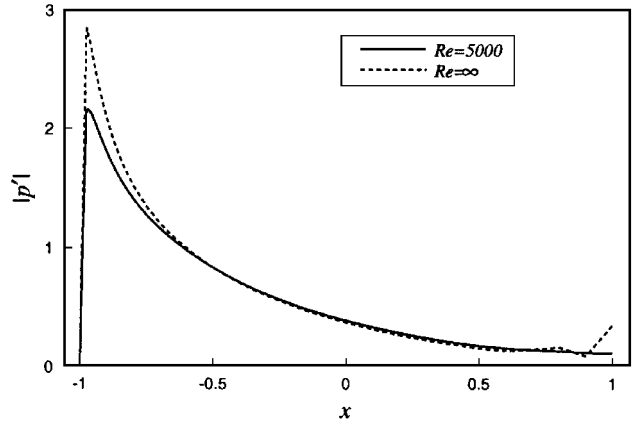

Fig. 13 Surface pressure magnitude variation with Reynolds number for a NACA0012 airfoil; $k = 1, M = 0.5$, and $\alpha = 0$ deg.

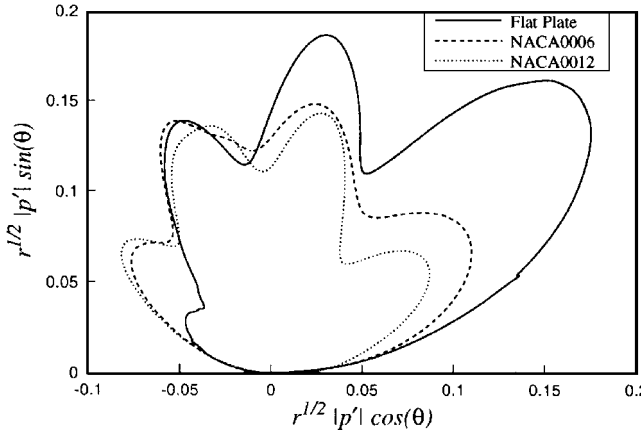

Fig. 14 Directivity variation with thickness; $k = 7.85, M = 0.5$, and $\alpha = 0$ deg.

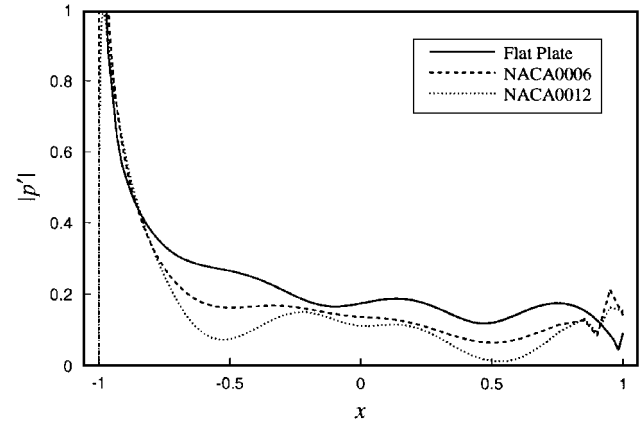

Fig. 15 Surface pressure magnitude variation with thickness; $k = 7.85$, $M = 0.5$, and $\alpha = 0$ deg.

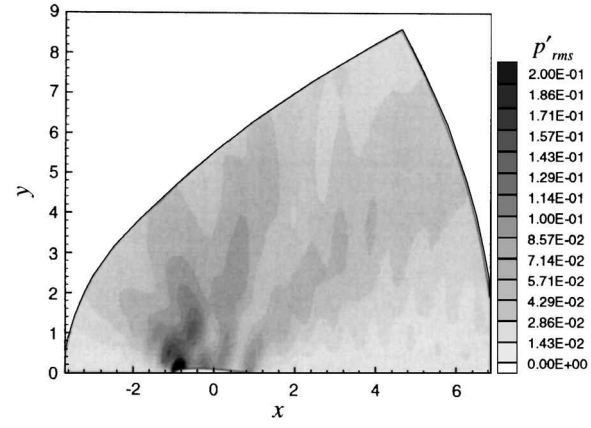

Fig. 16 NACA0012 airfoil rms pressure contours; $k = 7.85, M = 0.5$, and $\alpha = 0$ deg.

High Frequency

A higher frequency of $k = 7.85$ has been examined on a 161×257 grid. The solution on the coarser 81×129 mesh did not resolve all of the waves away from the body. However, similar lobed patterns are observed in both cases.

Figure 14 shows the effect of increasing thickness on the directivity. At $\alpha = 0$ deg the four-lobed pattern observed for the plate remains apparent for the NACA airfoils. However, the upstream lobe is increased, whereas the downstream lobes are reduced significantly. Most of the changes are evident for the NACA0006, indicating that the realistic mean flow and nose shape are the dominant factors for the observed changes from the flat plate case. Figure 15 demonstrates that the trend with thickness is also reproduced in the surface pressures. The surface pressures are modified more significantly by the thickness than the directivity, but some correspondence between them is still evident. The distribution of surface sources in the vertical direction for the finite thickness airfoils makes it more difficult to identify lobes in the directivity with a particular pattern in the surface pressure. As in the low-frequency case, there is a significant oscillation at the trailing edge. Although visible for the flat plate, it is considerably smaller in that case because a much finer grid is used to resolve more adequately the singularity.

Another difficulty with the higher-frequency case is visible in the rms pressure contours in Fig. 16. Downstream of the airfoil, the pattern exhibits considerable waviness. Although the propagation of the gust through the mean pressure discontinuity at the trailing edge and the difficulty in resolving all of the phenomena in that region could be responsible for the oscillations, the growth of instabilities in the gust may be important. A more detailed analysis of the flow downstream of the airfoil by the authors shows the existence of

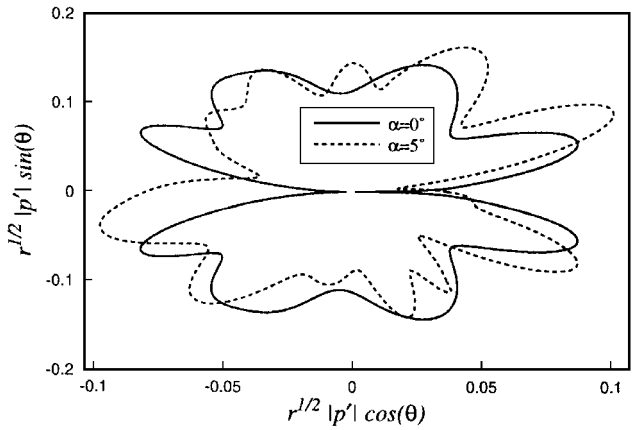

Fig. 17 Directivity variation with angle of attack for a NACA0012 airfoil; k = 7.85 and M = 0.5.

an interference pattern between the noise radiated from the airfoil surface and a disturbance emanating from the gust.[24] Most of this secondary noise source is limited to the region where the gust varies in y ($y \approx 1.5$), where instabilities are likely to grow. This is another instance of a physical mechanism making it difficult to simulate the idealized problem of an infinite gust.

The effect of angle of attack is also examined, but the results are more difficult to interpret. The directivity is given in Fig. 17. Augmentation and suppression of the radiated noise cannot always be related directly to the pressure and suction sides as in the low-frequency case. However, an examination of frequencies from $k = 1$ to $k = 15$ seems to indicate that suppression is more likely on the suction side. The directivity shape is also typically modified by the change in the mean flow associated with the effect of the angle of attack.

Conclusions

The calculations presented help to confirm that CAA techniques may be applied to realistic problems. Drastically different amplitudes between the mean flow and the acoustics have been captured. Realistic mean flows have been obtained in only a few minutes using a multigrid method and parallel computers. Greater improvements could be obtained by using implicit smoothing techniques and other preconditioners. Further enhancements in the convergence are needed to make three-dimensional problems more tractable. The efficiency of the unsteady simulations is even more important because they take considerably longer. An inviscid calculation on the 161×257 mesh requires 16 single-node hours. Inclusion of the viscous terms increases the CPU time by 50%.

The unsteady simulations of the radiated noise generated by plane, vortical gusts encountering thick airfoils are in general agreement with the work of Atassi et al.[20] The same trends with thickness and angle of attack have been observed. However, the numerical directivities are limited by the grid size and need to be extended to the far field using a Kirchhoff technique. Furthermore, the abrupt change in the boundary condition in the vicinity of the trailing edge gives rise to a pressure jump in the mean flow and spurious oscillations in the unsteady flow. These difficulties are accentuated by the seven-point, spatial-discretization stencil. More work is necessary in the inviscid flow cases to develop conditions to model the flow in this region adequately without resorting to an inordinately fine mesh.

Viscous effects have been shown to smooth the flow in the vicinity of the trailing edge without altering the radiated noise significantly. However, finer meshes are required. Furthermore, the viscous wake is unstable. At $k = 7.85$, gust-triggered instabilities in the wake grew rapidly and resulted in large variations in the mean flow. The radiation boundary conditions are not designed for such variations and generated large reflections. Even in inviscid cases, some spreading of the vorticity in the region where the gust varies in y has been observed. Thus, more work is necessary to simulate the idealized problem properly. However, it is more important to allow for and accommodate the growth rates of the instabilities in the gust and wake so that more realistic interaction problems may be performed with confidence.

Acknowledgments

This research was supported in part by the NASA Langley Research Center under Grant NAG-1-1479. The Technical Monitor is J. S. Preisser. The use of the computational resources of the National Aerospace Simulation High Performance Computing and Communications program and Pennsylvania State University is also acknowledged.

References

[1]Lockard, D. P., and Morris, P. J., "A Parallel Implementation of a Computational Aeroacoustic Algorithm for Airfoil Noise," *Journal of Computational Acoustics* (to be published); also AIAA Paper 96-1754, May 1996.

[2]Hardin, J. C., and Hussaini, M. Y. (eds.), *Computational Aeroacoustics*, Springer–Verlag, Berlin, 1993, pp. 313–376.

[3]Anderson, D. A., Tannehill, J. C., and Pletcher, R. H., *Computational Fluid Mechanics and Heat Transfer*, Taylor and Francis, New York, 1984, pp. 190, 254, 255

[4]Lockard, D. P., "Simulations of the Loading and Radiated Sound of Airfoils and Wings in Unsteady Flow Using Computational Aeroacoustics and Parallel Computers," Ph.D. Thesis, Dept. of Aerospace Engineering, Pennsylvania State Univ., University Park, PA, Aug. 1997.

[5]Hirsch, C., *Numerical Computation of Internal and External Flows*, Vol. 2, Wiley, New York, 1990, pp. 334–337, 346, 347.

[6]Hu, F. Q., Hussaini, M. Y., and Manthey, J., "Low-Dissipation and -Dispersion Runge–Kutta Schemes for Computational Aeroacoustics," *Journal of Computational Physics*, Vol. 124, No. 1, 1996, pp. 177–191.

[7]Tam, C. K. W., and Webb, J. C., "Dispersion-Relation-Preserving Finite Difference Schemes for Computational Aeroacoustics," *Journal of Computational Physics*, Vol. 107, No. 2, 1993, pp. 262–281.

[8]Lockard, D. P., Brentner, K. S., and Atkins, H. L., "High-Accuracy Algorithms for Computational Aeroacoustics," *AIAA Journal*, Vol. 33, No. 2, 1995, pp. 246–251.

[9]Jameson, A., Schmidt, W., and Turkel, E., "Numerical Solution of the Euler Equations by Finite-Volume Methods Using Runge–Kutta Time-Stepping Schemes," AIAA Paper 81-1259, June 1981.

[10]Tam, C. K. W., and Dong, Z., "Radiation and Outflow Boundary Conditions for Direct Computation of Acoustic and Flow Disturbances in a Nonuniform Mean Flow," CEAS/AIAA Paper 95-007, June 1995.

[11]Thompson, K. W., "Time-Dependent Boundary Conditions for Hyperbolic Systems, II," *Journal of Computational Physics*, Vol. 89, No. 2, 1989, pp. 439–461.

[12]Bayliss, A., and Turkel, E., "Far Field Boundary Conditions for Compressible Flow," *Journal of Computational Physics*, Vol. 48, No. 2, 1982, pp. 182–199.

[13]Jameson, A., "Multigrid Algorithms for Compressible Flow Calculations," *Multigrid Methods II, Proceedings of the 2nd European Conference on Multigrid Methods*, No. 1228, Lecture Notes in Mathematics, Springer–Verlag, Berlin, 1986, pp. 166–201.

[14]Chima, R. V., Turkel, E., and Schaffer, S., "Comparison of Three Explicit Multigrid Methods for the Euler and Navier–Stokes Equations," AIAA Paper 87-0602, Jan. 1987.

[15]Ozyoruk, Y., and Long, L. N., "Multigrid Acceleration of a High-Resolution Computational Aeroacoustics Scheme," *AIAA Journal*, Vol. 35, No. 3, 1997, pp. 428–433.

[16]Briggs, W. L., *A Multigrid Tutorial*, Society for Industrial and Applied Mathematics, Philadelphia, PA, 1987, Chap. 3.

[17]Davis, C. M., and Atassi, H. M., "Acoustic Radiation from a Lifting Airfoil in Nonuniform Subsonic Flows," *Computational Aero- and Hydro-Acoustics*, FED-Vol. 147, American Society of Mechenical Engineers, New York, 1993, pp. 41–46.

[18]Thomas, J. L., Krist, S., and Anderson, W., "Navier–Stokes Computations of Vortical Flows Over Low-Aspect-Ratio Wings," *AIAA Journal*, Vol. 28, No. 2, 1990, pp. 205–212.

[19]Atassi, H. M., Dusey, M., and Davis, C. M., "Acoustic Radiation from Thin Airfoils in Nonuniform Subsonic Flows," *AIAA Journal*, Vol. 31, No. 1, 1993, pp. 12–19.

[20]Atassi, H. M., Subramanian, S., and Scott, J. R., "Acoustic Radiation from Lifting Airfoils in Compressible Subsonic Flows," NASA TM-103650, Jan. 1990; also AIAA Paper 90-3911, Oct. 1990.

[21]Agarwal, R. K., and Huh, K. S., "Acoustic Radiation due to Gust–Airfoil Interaction in a Compressible Flow," CEAS/AIAA Paper 96-1755, May 1996.

[22]Myers, M. R., and Kerschen, E. J., "Influence of Incidence Angle on Sound Generation by Airfoils Interacting with a High-Frequency Gust," *Journal of Fluid Mechanics*, Vol. 292, June 1995, pp. 271–304.

[23]Howe, M. S., "Correlation of Lift and Thickness Noise Sources in Vortex–Airfoil Interaction," *Journal of Sound and Vibration*, Vol. 137, No. 1, 1990, pp. 1–7.

[24]Lockard, D. P., and Morris, P. J., "The Radiated Noise from Airfoils in Realistic Mean Flows," AIAA Paper 97-0286, Jan. 1997.

S. Glegg
Associate Editor